

# Electrodynamics and Ultimate SNR in Parallel MR Imaging

Florian Wiesinger, Peter Boesiger, and Klaas P. Pruessmann\*

**The purpose of this article is to elucidate inherent limitations to the performance of parallel MRI. The study focuses on the ultimate signal-to-noise ratio (SNR), which refers to the maximum SNR permitted by the electrodynamics of the signal detection process. Using a spherical model object, it is shown that the behavior of the ultimate SNR imposes distinct limits on the acceleration rate in parallel imaging. For low and moderate acceleration, the ultimate SNR performance is nearly optimal, with geometry factors close to 1. However, for high reduction factors beyond a critical value, the ultimate performance deteriorates rapidly, corresponding to exponential growth of the geometry factor. The transition from optimal to deteriorating performance depends on the electrodynamic characteristics of the detected RF fields. In the near-field regime, i.e., for low  $B_0$  and small object size, the critical reduction factor is constant and approximately equal to four for 1D acceleration in the sphere. In the far-field wave regime the critical reduction factor is larger and increases both with  $B_0$  and object size. Therefore, it is concluded that parallel techniques hold particular promise for human MR imaging at very high field. Magn Reson Med 52: 376–390, 2004. © 2004 Wiley-Liss, Inc.**

**Key words:** MRI; parallel imaging; SENSE; high field; electrodynamics; ultimate SNR

In recent years, parallel imaging with receiver coil arrays (1–5) has evolved into a practical and widely used variant of MRI. Exploiting the intrinsic encoding effect of coil sensitivity as a complement to gradient encoding, parallel acquisition permits reducing the density of  $k$ -space sampling. This advantage can be utilized to enhance MRI exams in manifold ways, such as for reducing scan time, improving resolution and coverage, suppressing artifacts, lowering RF power deposition, and even mitigating acoustic noise.

The main limiting factor in parallel imaging is the signal-to-noise ratio (SNR) of the resulting image data. For instance, for the parallel sensitivity encoding (SENSE) technique, the local SNR yield has been quantified as (3):

$$\text{SNR}^{\text{PI}} = \frac{\text{SNR}^{\text{full}}}{\sqrt{R} g}, \quad [1]$$

where  $\text{SNR}^{\text{PI}}$  denotes the SNR obtained with parallel imaging and  $\text{SNR}^{\text{full}}$  denotes the SNR that would be obtained

with conventional, full gradient encoding, using the same sequence and the same coil array. According to this relation, the SNR yield of parallel imaging is subject to two types of losses. The factor  $\sqrt{R}$  accounts for reduced intrinsic signal averaging when the  $k$ -space density is reduced by the factor  $R$ . The second loss term,  $g$ , is the local so-called geometry factor, which reflects the ability of the coil array to complement the reduced gradient encoding. This ability depends crucially on the number and geometrical configuration of the array elements.

As a consequence, the SNR yield of parallel imaging can be significantly improved by coil optimization. Typically, dedicated coil designs yield favorable  $g$  values up to reduction factors between three and four in one dimension (6–8). However, beyond this threshold dramatic increases in  $g$  are observed even with optimized arrays. These findings suggest that the reduction factor in parallel imaging is limited not only by array imperfection but also in a further, more fundamental fashion. This hypothesis has been the subject of several recent investigations (9–11).

The present work builds on Ref. 9. Its goal is to establish the inherent performance limits of parallel imaging and to put them into the perspective of the underlying physics. To this end, the concept of ultimate intrinsic SNR (12) is adopted and extended toward parallel acquisition. With this approach, the highest achievable relative SNR is determined for parallel imaging with varying  $B_0$ , object size, and reduction factor  $R$ . The resulting SNR data and the corresponding geometry factors reveal performance limits with a characteristic structure, which directly corresponds to the electrodynamics of MR signal detection.

## THEORY

In this section the problem of determining the ultimate intrinsic SNR in parallel MRI is cast into the form of a constrained minimization problem. First, the signal and noise amplitudes detected with an MR receiver coil are expressed in terms of the coil's hypothetical transmit fields, applying the principle of reciprocity. In the following part, the impact of parallel imaging reconstruction on the image SNR is incorporated using the concept of net sensitivity, which translates into a constraint on SNR optimization. A second constraint is then imposed according to the underlying physics, which require that the signal and noise sensitivity functions fulfill the Maxwell equations. The Maxwell constraint is incorporated by expanding the sensitivity functions in terms of a basis of Maxwell solutions. This expansion then permits expressing and solving the optimization problem with matrix notation, as described in the last part of the section.

### Signal and Noise Sensitivity

The basic determinants of the SNR in MRI are the signal voltage amplitude,  $v_s$ , and the root-mean-square (RMS)

Institute for Biomedical Engineering, University of Zurich and Swiss Federal Institute of Technology Zurich, Zurich, Switzerland.

Grant sponsors: EUREKA/KTI EI2061/4178.1 INCA-MRI and SEP Life Sciences TH7/02-2 of ETH Zurich "New MRI Techniques for the Assessment of Brain and Heart Function."

\*Correspondence to: Prof. Dr. Klaas P. Pruessmann, Institute for Biomedical Engineering, University and ETH Zurich, Gloriastrasse 35, CH-8092 Zurich, Switzerland. E-mail: pruessmann@biomed.ee.ethz.ch

Received 20 October 2003; revised 6 April 2004; accepted 7 April 2004.

DOI 10.1002/mrm.20183

Published online in Wiley InterScience (www.interscience.wiley.com).

© 2004 Wiley-Liss, Inc.

noise voltage,  $v_N$ , at the output of the detector. As the signal source, we consider the nuclear magnetic moment  $M_0$  at the position  $\mathbf{r}_0$ , precessing about the z-axis with the Larmor frequency  $\omega$ . Assuming steady-state oscillation and Faraday detection with a receiver coil, the principle of reciprocity (13–15) yields the signal voltage:

$$v_S = M_0 \mu(\mathbf{r}_0) \omega |H_x(\mathbf{r}_0) - iH_y(\mathbf{r}_0)|, \quad [2]$$

where  $\mu$  denotes the local magnetic permeability and  $i$  the imaginary unit.  $H_x$ ,  $H_y$  denote the complex amplitudes of the x- and y-components of the RF magnetic field that the coil generates when operated with unit input current of frequency  $\omega$ .

Among the various mechanisms that underlie noise in MR detection, we consider only the component caused by thermal agitation of charged particles in the object (16–18), following the reasoning previously given in Ref. 12. In the reciprocal view, this type of noise corresponds to losses associated with currents induced in the object. Other mechanisms, such as radiation loss or ohmic losses in the coil conductor, are neglected in the following as they can be diminished in principle by enhancing the coil technology. For a given receiver bandwidth BW, the RMS noise voltage is then given by (18):

$$v_N = \sqrt{4BWk_B T \int_{\text{object}} \sigma(\mathbf{r}) |\mathbf{E}(\mathbf{r})|^2 d^3\mathbf{r}}, \quad [3]$$

where  $k_B$  denotes the Boltzmann constant,  $T$  the absolute temperature,  $\sigma$  the conductivity of the sample, and  $\mathbf{E}(\mathbf{r})$  the complex amplitude vector of the RF electric field generated by the receiver coil when driven with unit input current of frequency  $\omega$ .

Equations [2, 3] describe the reception behavior of a given detector coil in terms of its hypothetical transmit fields. The transverse components of the magnetic transmit field  $\mathbf{H}(\mathbf{r})$  characterize MR signal reception from position  $\mathbf{r}$ . The expression  $H_x(\mathbf{r}) - iH_y(\mathbf{r})$  is therefore referred to as the coil's signal sensitivity in the scope of the present work. Similarly, the electric transmit field,  $\mathbf{E}(\mathbf{r})$ , is viewed as the coil's noise sensitivity.

### Image Formation and Spatial Response

In each sample of the induced voltage, the resonance signal from  $\mathbf{r}_0$  is entangled with signal contributions from the entire object, requiring spatial encoding and a reconstruction step for the purpose of imaging. For parallel imaging, the spatial encoding is performed by combining gradient switching with the encoding effect of multiple receiver coil sensitivities. In the scope of the present work, acquisition and reconstruction are modeled according to Cartesian SENSE with weak reconstruction, as described in Ref. 3. According to this method, gradient encoding is assumed to cover a Cartesian  $k$ -space grid with reduced density relative to the nominal FOV.

The first step in this type of SENSE reconstruction is discrete Fourier transform for each coil element, yielding single-coil images with reduced FOV and aliasing artifact. The aliasing effect can be described comprehensively by the so-called spatial response function (SRF), which re-

flects the spatial weighting of signal contributions in a given pixel value. In each of the single-coil images the spatial response depends on the coil's signal sensitivity and the point-spread function (PSF) of Fourier encoding and reconstruction. For the coil element with index  $\gamma$  and a pixel at position  $\mathbf{r}_0$ , the SRF reads:

$$\text{SRF}^\gamma(\mathbf{r}) = (H_x^\gamma(\mathbf{r}) - iH_y^\gamma(\mathbf{r})) \text{PSF}_{\text{Fourier}}(\mathbf{r}_0 - \mathbf{r}). \quad [4]$$

The concept of spatial response is illustrated in Fig. 1, showing SRFs of a central pixel for four coils, assuming  $k$ -space undersampling in one dimension by a factor of  $R = 3$ . According to Cartesian scanning, the PSF is formed by a series of sinc peaks, with a spacing of  $\text{FOV}/R$ . Due to 3-fold undersampling, the PSF exhibits three main peaks within the object. One of these peaks is centered at position  $\mathbf{r}_0$ , reflecting the desired response, while the others reflect aliasing contributions. Weighting by each coil's signal sensitivity according to Eq. [4] results in individually varying peak heights of the SRF. Hence, each pixel in the aliased single-coil images represents the sum of three individually weighted contributions. Note that signal sensitivity, SRF, and single coil images are complex-valued, Fig. 1 showing only moduli. Note also that the same view holds for undersampling in multiple  $k$ -space dimensions, where the aliasing peaks form a higher-dimensional grid (19).

### Net Coils

For any given  $\mathbf{r}_0$  and undersampling scheme, let the aliasing positions be given by  $\mathbf{r}_1, \mathbf{r}_2, \dots, \mathbf{r}_N$  in arbitrary order. In each single-coil image, the signal from these positions is entangled in a single aliased pixel. In SENSE reconstruction, an unaliased pixel value for each of the involved positions is obtained by suitable linear combination of the aliased single-coil pixel values. The spatial response of the reconstructed pixel is obtained by likewise linearly combining the corresponding single coil SRFs. For the pixel with index  $\rho = 0, \dots, N$ , the resulting net SRF reads:

$$\text{SRF}^{\text{net},\rho}(\mathbf{r}) = \sum_{\gamma} c_{\rho,\gamma} \text{SRF}^\gamma(\mathbf{r}), \quad [5]$$

where  $c_{\rho,\gamma}$  denotes the coefficient used for weighting the coil  $\gamma$  in SENSE reconstruction. Inserting Eq. [4] and defining the net magnetic transmit field:

$$\mathbf{H}^{\text{net},\rho}(\mathbf{r}) = \sum_{\gamma} c_{\rho,\gamma} \mathbf{H}^\gamma(\mathbf{r}), \quad [6]$$

one obtains:

$$\text{SRF}^{\text{net},\rho}(\mathbf{r}) = (H_x^{\text{net},\rho}(\mathbf{r}) - iH_y^{\text{net},\rho}(\mathbf{r})) \text{PSF}_{\text{Fourier}}(\mathbf{r}_\rho - \mathbf{r}). \quad [7]$$

In the net SRFs, unaliasing is reflected by the suppression of aliasing PSF peaks. Weak SENSE reconstruction ensures that the net signal sensitivity is equal to one at the reconstructed position  $\mathbf{r}_\rho$ , and equal to zero at the aliasing positions (see Fig. 1). Formally, this is expressed as:

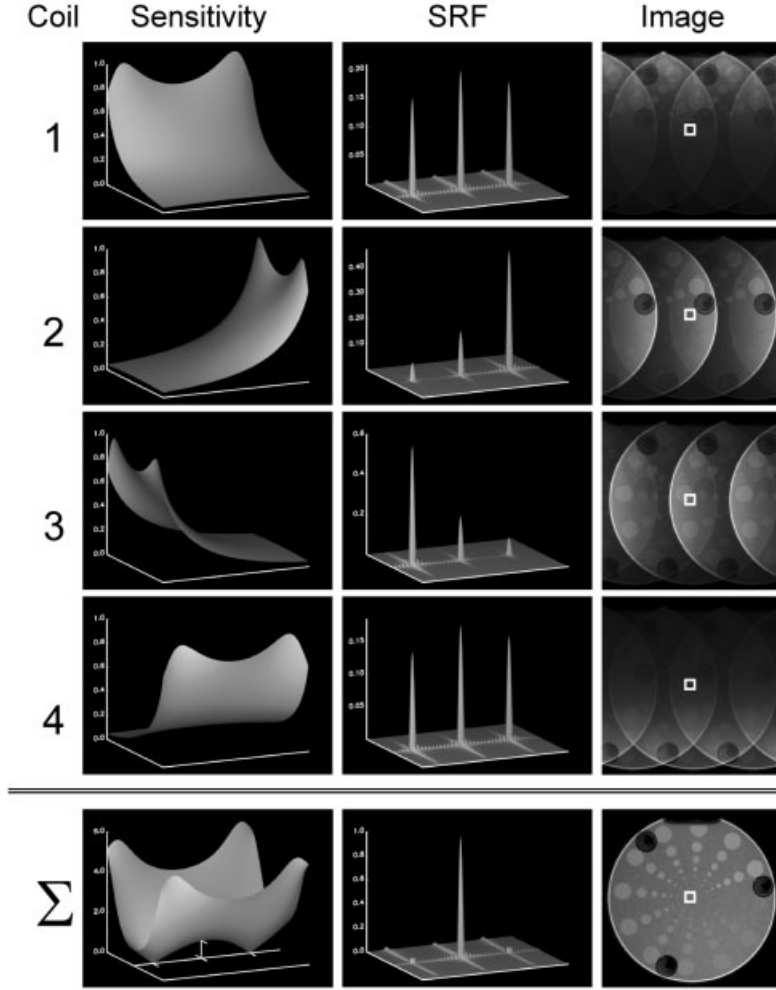


FIG. 1. Spatial response and net sensitivity in Cartesian parallel imaging with  $R = 3$ . Rows 1–4 illustrate signal aliasing in a central pixel for the four different elements of a receiver coil array. The left column shows each coil's spatial sensitivity in the image plane. The sensitivities introduce a spatial weighting in the multiple peaks of the individual spatial response functions (SRF, middle column). Correspondingly, the aliasing contributions in the single coil images are individually weighted (right column). Parallel imaging reconstruction of the central pixel amounts to a linear combination ( $\Sigma$ ) of the aliased pixel values. The same linear combination can equivalently be performed with the coil sensitivities, yielding the net sensitivity for reconstructing this pixel. The net sensitivity has zeros where aliasing contributions need to be suppressed. Consequently, the net SRF exhibits only the desired single peak. In the context of ultimate SNR, the net sensitivity is of special significance because it is subject to the same electrodynamic limitations as actual coil sensitivities.

$$H_x^{\text{net},\rho}(\mathbf{r}_{\rho'}) - iH_y^{\text{net},\rho}(\mathbf{r}_{\rho'}) = \delta_{\rho,\rho'} \quad \text{for } \rho, \rho' = 0, \dots, N, \quad [8]$$

where  $\delta$  denotes the Kronecker delta.

The strength of the concept of net sensitivity is that it casts the problem of quantifying noise propagation in SENSE reconstruction into the realm of electrodynamics. In a thought experiment, replace the coil array by a single net coil, which is obtained by linear combination of the original array elements, using the coefficients  $c_{\rho,\gamma}$ . Due to the linearity of electrodynamics, such a coil will have the magnetic transmit field given in Eq. [6] and the electric transmit field:

$$\mathbf{E}^{\text{net},\rho}(\mathbf{r}) = \sum_{\gamma} c_{\rho,\gamma} \mathbf{E}^{\gamma}(\mathbf{r}). \quad [9]$$

The net coil's signal sensitivity conforms to Eq. [8], hence mere Fourier transform from net coil data will yield a nonaliased pixel value for  $\mathbf{r}_{\rho}$ , despite undersampling. Furthermore, since Fourier transform is likewise linear, this pixel value will have the exact same signal and noise levels as would have been obtained with the original procedure. Hence, for assessing the maximum SNR achievable with SENSE imaging, it is sufficient to identify the net

transmit fields that maximize the SNR in standard Fourier reconstruction, while fulfilling condition [8].

#### Signal-to-Noise Ratio

Combining Eqs. [2, 3, 8] for the net coil and dividing the resulting signal and noise levels yields:

$$\text{SNR}(\mathbf{r}_{\rho}) = \frac{M_0 \mu(\mathbf{r}_{\rho}) \omega n_K}{\sqrt{4BWk_B T n_K \int_{\text{object}} \sigma(\mathbf{r}) |\mathbf{E}^{\text{net},\rho}(\mathbf{r})|^2 d^3 \mathbf{r}}}. \quad [10]$$

Here, the number of  $k$ -space samples,  $n_K$ , is included to account for the signal summation performed by the Fourier transform. When varying the object size, it shall be assumed that the FOV and the slice thickness scale along with the object. Hence, the relevant magnetic moment  $M_0$  in Eq. [10] is proportional to  $\text{FOV}^3$ . Furthermore, both  $M_0$  and the Larmor frequency  $\omega$  are proportional to  $B_0$  under typical in vivo MRI conditions. The scaling factors are neglected in the following, along with further terms which are held constant in the scope of this work. This leads to the relative SNR:

$$\zeta(\mathbf{r}_{\rho}) = \frac{\mu(\mathbf{r}_{\rho}) B_0^2 \text{FOV}^3 \sqrt{n_K}}{\sqrt{\int_{\text{object}} \sigma(\mathbf{r}) |\mathbf{E}^{\text{net},\rho}(\mathbf{r})|^2 d^3 \mathbf{r}}}, \quad [11]$$

which is an accurate comparative SNR measure for varying  $B_0$ , object size, transmit fields, material properties, and SENSE factors. Note that the signal and noise sensitivities are implicit functions of the Larmor frequency and the material properties. The latter are themselves frequency-dependent, thus adding multiple implicit dependencies on  $B_0$ .

According to the previous considerations, ultimate local SNR in SENSE imaging is characterized by a maximum of  $\zeta(\mathbf{r}_p)$  under the unfolding constraint [8]. For a given object,  $B_0$ , and  $k$ -space grid, maximizing  $\zeta(\mathbf{r}_p)$  is hence equivalent to the constrained minimization of the denominator in Eq. [11]:

$$\int_{\text{object}} \sigma(\mathbf{r}) |\mathbf{E}^{\text{net},\rho}(\mathbf{r})|^2 d^3\mathbf{r} \rightarrow \min. \quad [12]$$

### Maxwell Equations

Without additional constraints, the noise sensitivity could simply be set to zero, yielding infinite SNR. However, this is not an option because signal and noise sensitivity are coupled by the laws of electrodynamics. In order to simplify the latter, two assumptions are made in the following. First, the object to be imaged is assumed to have scalar, homogeneous dielectric constant  $\epsilon$ , magnetic permeability  $\mu$ , and conductivity  $\sigma$ . Second, all receiver coils are assumed to be placed outside the object, which holds for most diagnostic MRI procedures with the exception of interventional or endocavitary studies. Under these conditions, the signal and noise sensitivities of each coil are governed by the source-free Maxwell equations (20):

$$\begin{aligned} \nabla \cdot \mathbf{E}(\mathbf{r}, t) &= 0, \quad \nabla \times \mathbf{E}(\mathbf{r}, t) = -\mu \frac{\partial \mathbf{H}(\mathbf{r}, t)}{\partial t} \\ \nabla \cdot \mathbf{H}(\mathbf{r}, t) &= 0, \quad \nabla \times \mathbf{H}(\mathbf{r}, t) = \epsilon \frac{\partial \mathbf{E}(\mathbf{r}, t)}{\partial t} + \sigma \mathbf{E}(\mathbf{r}, t) \end{aligned}, \quad [13]$$

where  $\Delta$  denotes the gradient operator. Assuming steady-state oscillation at the Larmor frequency with the time dependency  $\exp(-i\omega t)$ , the Maxwell equations permit separating spatial and temporal evolution. For  $\omega \neq 0$ , the spatial dependence is governed by the reduced, equivalent set of equations (20):

$$(\Delta + k_0^2) \mathbf{H}(\mathbf{r}) = 0, \quad [14]$$

$$\nabla \cdot \mathbf{H}(\mathbf{r}) = 0, \quad [15]$$

$$\mathbf{E}(\mathbf{r}) = \frac{1}{\sigma - i\omega\epsilon} \nabla \times \mathbf{H}(\mathbf{r}), \quad [16]$$

where  $\nabla$  denotes the Laplace operator and  $k_0$  the complex wave number given by:

$$k_0^2 = \omega\mu(\omega\epsilon + i\sigma). \quad [17]$$

As such, these conditions form an awkward constraint in SNR optimization. However, note that the Maxwell equa-

tions are linear and homogeneous in this form. Hence, their solutions form a linear space and each linear combination of solutions is again a solution. Therefore the constraints [14–16] translate directly to the hypothetical net coil, which is a linear combination of actual coils. Furthermore, these constraints can be enforced by expanding the net coil in terms of a complete basis of the solution space:

$$\begin{aligned} \mathbf{E}^{\text{net},\rho}(\mathbf{r}) &= \sum_m w_{\rho,m} \boldsymbol{\alpha}_m(\mathbf{r}) \\ \mathbf{H}^{\text{net},\rho}(\mathbf{r}) &= \sum_m w_{\rho,m} \boldsymbol{\beta}_m(\mathbf{r}), \end{aligned} \quad [18]$$

where  $\boldsymbol{\alpha}_m(\mathbf{r})$ ,  $\boldsymbol{\beta}_m(\mathbf{r})$  are electric and magnetic vector basis functions, counted by the index  $m$ , and  $w_{\rho,m}$  are complex weighting coefficients. Using the expansion [18], the problem of fulfilling the Maxwell constraints is transformed into the unconstrained choice of the weighting coefficients  $w_{\rho,m}$ .

### Matrix Description and Solution

Based on the expansion [18], the remaining constraint [8] is restated as:

$$\sum_m w_{\rho,m} (\beta_{m,x}(\mathbf{r}_{p'}) - i\beta_{m,y}(\mathbf{r}_{p'})) = \delta_{\rho,p'}. \quad [19]$$

Assembling the  $w_{\rho,m}$  in the weighting matrix  $W$  and introducing the signal sensitivity matrix  $S$ :

$$S_{m,\rho} = \beta_{m,x}(\mathbf{r}_\rho) - i\beta_{m,y}(\mathbf{r}_\rho), \quad [20]$$

the constraining Eq. [8] can be expressed more compactly as:

$$WS = \text{Id}, \quad [21]$$

where  $\text{Id}$  denotes the  $(N+1) \times (N+1)$  identity matrix. Similarly, the functional to be minimized (Eq. [12]) can be expressed in matrix notation. Defining the noise covariance matrix  $\Psi$  as:

$$\Psi_{mm'} = \sigma \int_{\text{object}} \boldsymbol{\alpha}_m(\mathbf{r}) \boldsymbol{\alpha}_{m'}^*(\mathbf{r}) d^3\mathbf{r}, \quad [22]$$

the functional reads:

$$\int_{\text{object}} \sigma |\mathbf{E}^{\text{net},\rho}(\mathbf{r})|^2 d^3\mathbf{r} = (W\Psi W^H)_{\rho,\rho}, \quad [23]$$

where the superscript  $H$  denotes the complex conjugate transpose. SNR optimization is thus reduced to identifying optimal entries for the weighting matrix  $W$  that minimize  $(W\Psi W^H)_{\rho,\rho}$  for each pixel  $\rho$ , while fulfilling Eq. [21]. Note that for each pixel the optimization involves only the corresponding row of  $W$  (and column of  $W^H$ ), making the problem pixel-wise-independent. The minimization can



therefore be performed simultaneously for all pixels involved by minimizing the trace of  $\mathbf{W}\Psi\mathbf{W}^H$ .

This can be done using Lagrange multipliers, as in Ref. 3. Alternatively, it can be cast into the form of a minimum-norm problem as described in Appendix A. Either approach yields:

$$\mathbf{W}_{\min} = (\mathbf{S}^H \Psi^{-1} \mathbf{S})^{-1} \mathbf{S}^H \Psi^{-1}. \quad [24]$$

This weighting matrix defines an optimal net coil for each of the pixel positions  $\mathbf{r}_0, \mathbf{r}_1, \dots, \mathbf{r}_N$ . Inserting it into Eq. [23] and substituting into Eq. [11] yields a feasible expression for the ultimate SNR:

$$\zeta(\mathbf{r}_0) = \frac{\mu(\mathbf{r}_0) B_0^2 \text{FOV}^3 \sqrt{n_K}}{\sqrt{[(\mathbf{S}^H \Psi^{-1} \mathbf{S})^{-1}]_{0,0}}}, \quad [25]$$

where the pixel index was set to  $\rho = 0$ , which corresponds to the original target position  $\mathbf{r}_0$  according to the definition preceding Eq. [5].

For a given object, key parameters that influence the SNR are  $\mathbf{r}_0$  and  $B_0$ , as well as the mode and degree of  $k$ -space undersampling.  $B_0$  determines  $\omega$  and thus implicitly the electrodynamic material properties and the basis set  $\boldsymbol{\alpha}_m(\mathbf{r}), \boldsymbol{\beta}_m(\mathbf{r})$ . Thereby,  $B_0$  also co-determines the matrices  $\Psi$  and  $\mathbf{S}$ . The target position  $\mathbf{r}_0$  and the undersampling scheme determine the aliasing positions, hence co-determining the matrix  $\mathbf{S}$ . Based on the ultimate SNR, the ultimate geometry factor is defined in analogy to Eq. [1] as:

$$g(\mathbf{r}_0) = \frac{1}{\sqrt{R}} \frac{\zeta^{\text{full}}(\mathbf{r}_0)}{\zeta^{\text{PI}}(\mathbf{r}_0)} \geq 1. \quad [26]$$

For this expression,  $\zeta^{\text{full}}$  and  $\zeta^{\text{PI}}$  are both calculated using Eq. [25]; however, with different  $k$ -space sampling.  $\zeta^{\text{full}}$  is obtained with full sampling. This leads to no aliasing, hence the sensitivity matrix  $\mathbf{S}$  has only one column in this case.  $\zeta^{\text{PI}}$  is obtained with reduced  $k$ -space sampling with the undersampling factor  $R$ . The resulting aliasing is reflected in a matrix  $\mathbf{S}$  with multiple columns. Note that different degrees of reduction affect only the matrix  $\mathbf{S}$ , while the noise covariance matrix  $\Psi$  does not change.

### Complete Coil Arrays

Note the close correspondence between Eqs. [6, 9] and Eq. [18]. It illustrates that creating a net coil follows the same rules, be it either from actual coils, as done in SENSE reconstruction, or from a complete basis set. This prompts the concept of hypothetical “complete” coil arrays, whose elements’ transmit fields span the entire solution space of the Maxwell equations. According to the considerations in this section, a complete array would always yield the ultimate SNR, both in parallel and conventional MRI. This is also illustrated by the formal identity of Eq. [24] and the formula for Cartesian SENSE reconstruction given in Ref. 3. According to this finding, calculating the ultimate SNR for SENSE imaging is essentially equivalent to SENSE reconstruction from data obtained with a hypothetical complete coil array. This is important because it translates

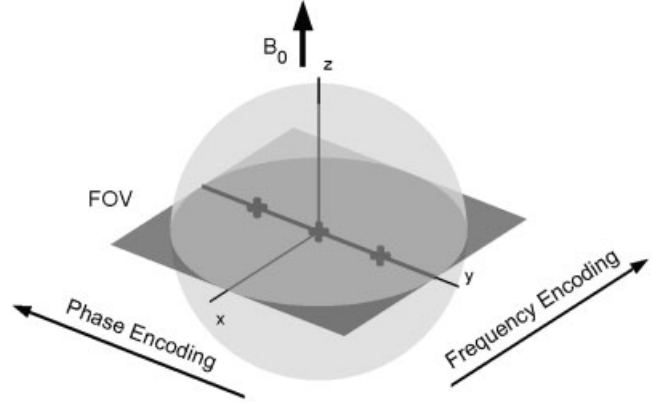


FIG. 2. Model setup for studies of ultimate SNR and g factor in Cartesian parallel imaging of a spherical object. The FOV is a circumscribed, concentric square with side length equal to the diameter of the sphere. The  $k$ -space sampling density was reduced in the phase encoding direction by the reduction factor  $R$ . In the shown case,  $R = 3.8$  results in 3-fold aliasing of the central pixel.

to any linear reconstruction algorithm, including, e.g., reconstruction from non-Cartesian  $k$ -space data.

### MATERIALS AND METHODS

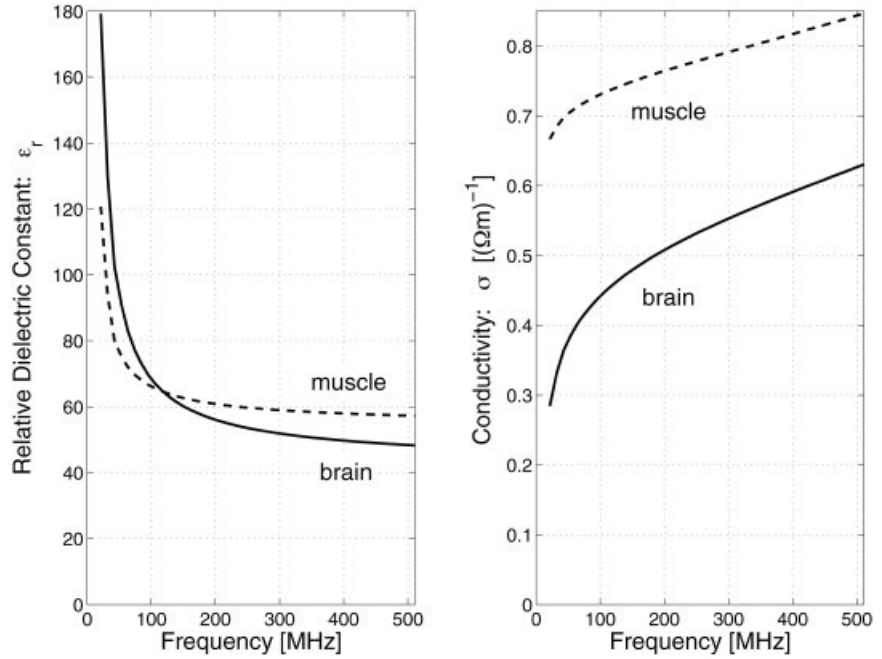
The numerical complexity of evaluating Eqs. [25, 26] depends strongly on the modeled object geometry and the specific choice of the Maxwell basis functions [18]. For the practical part of the present work, the object was assumed to be a sphere, favoring a multipole expansion into spherical harmonics. This expansion and its numerical implications are detailed in Appendix B. Briefly, within a spherical object the chosen spherical harmonics are mutually orthogonal, making the calculation and inversion of the noise covariance matrix  $\Psi$  very efficient and robust. Nevertheless, numerical integration is necessary for determining its diagonal elements. Very importantly, the multipole expansion matches the spherical object also in the sense that it permits a relatively compact representation of the optimal net detection fields. That is, good approximations of the ultimate SNR can be obtained with a moderate number of basis functions.

Based on these choices, the calculation of ultimate SNR and g factors in SENSE imaging was implemented on a standard PC, using MatLab (MathWorks, Natick, MA).

### Model Specifications

Ultimate SNR calculations were performed for 2D Cartesian parallel imaging with undersampling only in the phase-encoding direction. Within the MatLab program, a specific calculation is prescribed as follows. The basic geometric specifications are the size of the sphere and the angulation of the FOV relative to the  $B_0$  axis. The FOV is generally assumed to be a concentric square with side length equal to the sphere’s diameter.  $k$ -Space sampling is determined by choosing the phase-encoding direction and the undersampling factor  $R$ . The  $z$ -axis of the coordinate system is generally parallel to  $B_0$ . A typical configuration with  $R = 3.8$  is sketched in Fig. 2. Based on the choice of

FIG. 3. Frequency dependence of material properties according to Gabriel et al. (21). Left: Relative dielectric constant  $\epsilon_r$ . Right: conductivity  $\sigma$ . Solid lines: average in vivo brain tissue. Dashed lines: average in vivo muscle tissue for comparison.



$B_0$ , the Larmor frequency  $\omega$  is determined, using the gyro-magnetic ratio of water protons ( $\gamma = 42.576$  MHz/T).

Unless stated otherwise, the frequency-dependent values of the conductivity  $\sigma$  and the relative dielectric constant  $\epsilon_r$  were set according to average in vivo brain conditions (21). Figure 3 shows plots of the used  $\sigma$  and  $\epsilon_r$  values vs.  $B_0$ , along with average in vivo values for muscle tissue for comparison. According to common in vivo situations, the relative magnetic permeability  $\mu_r$  was generally set to unity. For several representative field strengths, the corresponding frequencies, material constants, and wavelengths are listed in Table 1. Finally, the spherical harmonic basis functions are specified by choosing the expansion order  $l_{\max}$ . The resulting number of vector basis functions is  $2 \cdot (l_{\max} + 1)^2$  (see Appendix B).

## RESULTS

### Numerical Convergence

For the subsequent numerical study it was crucial that the finite multipole expansion be sufficiently accurate. This was ensured by an initial convergence analysis, establishing how fast the ultimate SNR approaches a limit as the order of the expansion,  $l_{\max}$ , increases. Figure 4 shows the results of this investigation for a few representative situations. In order to facilitate comparisons between different parameter sets, the ultimate SNR (Eq. [25]) was normalized

by its value for  $l_{\max} = 10$ . Then the inverse of the normalized SNR was plotted vs. the number of basis functions  $2 \cdot (l_{\max} + 1)^2$ . Data are shown for each combination of three different target positions, two extreme field strengths ( $B_0 = 1$  T,  $B_0 = 10$  T), and two extreme reduction factors ( $R = 1$ ,  $R = 10$ ). The image plane was transverse, with an FOV of 0.3 m. In all cases the SNR clearly converges within the covered range of up to 20,000 basis functions ( $l_{\max} \approx 100$ ).

As may be expected, the required expansion order increases as the reduction factor grows and as the reconstruction point approaches the surface of the sphere. These results show that a multipole expansion of order in the range of 80 is sufficient for determining the ultimate SNR for  $\mathbf{r}_0$ ,  $B_0$ , and  $R$  within the ranges spanned by this analysis. The expansion order was hence set to  $l_{\max} = 80$  for all following calculations. The results also suggest that higher-order expansion is necessary for  $\mathbf{r}_0$  very close to the surface. Therefore, all subsequent SNR calculations were restricted to a spherical volume slightly smaller than the actual object (diameter =  $0.95 \cdot \text{FOV}$ ).

### Ultimate SNR for $R = 1$

As suggested by Eq. [26], the ultimate SNR in parallel imaging may be characterized by the SNR that can be achieved with full Fourier encoding,  $\zeta^{\text{full}}$ , and by the geometry factor. First,  $\zeta^{\text{full}}$  is studied here by setting  $R = 1$ .

Table 1

Relative Dielectric Constant  $\epsilon_r$ , Conductivity  $\sigma$ , and Resulting Wavelength  $\lambda$  in Average Brain Tissue (According to Ref. 21)

$B_0$ [T]	1	3	5	7	9	11
$\omega/2\pi$ [MHz]	42.6	127.7	212.9	298.1	383.2	468.4
$\epsilon_r^{\text{brain}}$	102.5	63.1	55.3	52	50	48.8
$\sigma^{\text{brain}}$ [ $1/\Omega m$ ]	0.36	0.46	0.51	0.55	0.59	0.62
$\lambda^{\text{brain}}$ [cm]	58.8	26.8	17.8	13.3	10.7	8.9

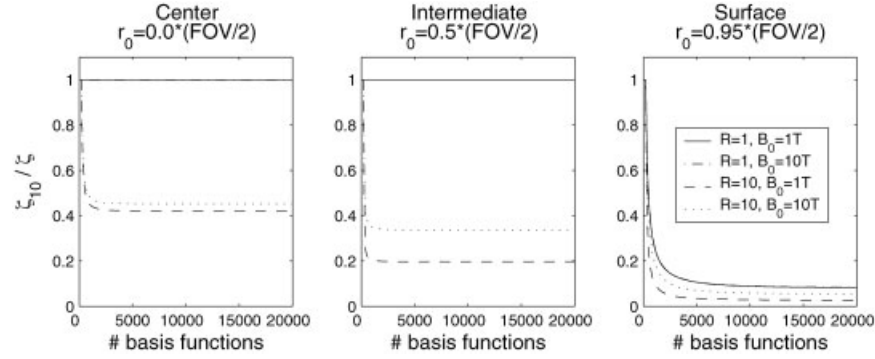


FIG. 4. Convergence of the calculated ultimate SNR as a function of the number of basis functions  $2 \cdot (l_{\max} + 1)^2$ , where  $l_{\max}$  denotes the order of the spherical harmonic expansion. The ultimate SNR  $\zeta$  was calculated for three different positions in the sphere (center, intermediate radius, beneath the surface), two extreme reduction factors ( $R = 1, R = 10$ ) and two extreme field strengths ( $B_0 = 1\text{ T}, B_0 = 10\text{ T}$ ). The plots show the inverse of  $\zeta$ , after normalization by its value for  $l_{\max} = 10$ . At  $R = 1$  the convergence behavior is virtually equal for 1 T and 10 T. Therefore, the solid and dash-dotted lines coincide. In all cases, the SNR clearly converges within the covered range of up to 20,000 basis functions ( $l_{\max} \approx 100$ ). Based on these results, the expansion order was generally set to  $l_{\max} = 80$ .

Given the spherical symmetry of the object, one may expect that  $\zeta^{\text{full}}$  should exhibit spherical symmetry as well. However, the spherical symmetry is broken by the direction of  $B_0$ , which determines how the magnetic RF field components combine in forming the signal sensitivity (Eq. [2]). Therefore, the only symmetry of  $\zeta^{\text{full}}$  is rotation symmetry about the  $B_0$  direction. As a consequence, the radial dependence of  $\zeta^{\text{full}}$  along the z-axis differs slightly from that in the transverse plane.

Figure 5 shows the radial dependence of the ultimate SNR for  $R = 1$  ( $\zeta^{\text{full}}$ ) for sphere sizes between 0.1 m and 0.5 m and  $B_0$  between 1 T and 10 T. The ultimate SNR in the transverse plane,  $\zeta_t^{\text{full}}$ , increases with increasing field strength and towards the surface of the sphere. In particular, the minimum of the ultimate SNR is always located in the center of the sphere.

The bottom row of Fig. 5 shows the relative deviation of the ultimate SNR along the z axis,  $\zeta_z^{\text{full}}$ , from that in the transverse plane for the same combinations of FOV and  $B_0$ . Starting from 1 in the center of the sphere, the ratio appears to always converge towards  $\sim 0.82$  at the surface. That is, the ultimate SNR at the sphere's poles is about 82% of that at its equator. For intermediate radii, the behavior of  $\zeta_z^{\text{full}}/\zeta_t^{\text{full}}$  is generally less systematic, showing values larger and smaller than 1 and partly assuming local extrema. At low values of FOV and  $B_0$ , the ratio is almost independent of the two parameters and decreases continuously towards the surface.

The next part of the study focused on the dependence of the ultimate SNR on the field strength  $B_0$ . In previous studies, the SNR was found to be approximately linear in  $B_0$  for low  $B_0$ , while changing to higher power growth for higher  $B_0$  (12,22,23). That is, in each  $B_0$  regime the SNR approximately obeys a law of the form:

$$\zeta^{\text{full}} = c B_0^n \Leftrightarrow \log(\zeta^{\text{full}}) = \log(c) + n \log(B_0), \quad [27]$$

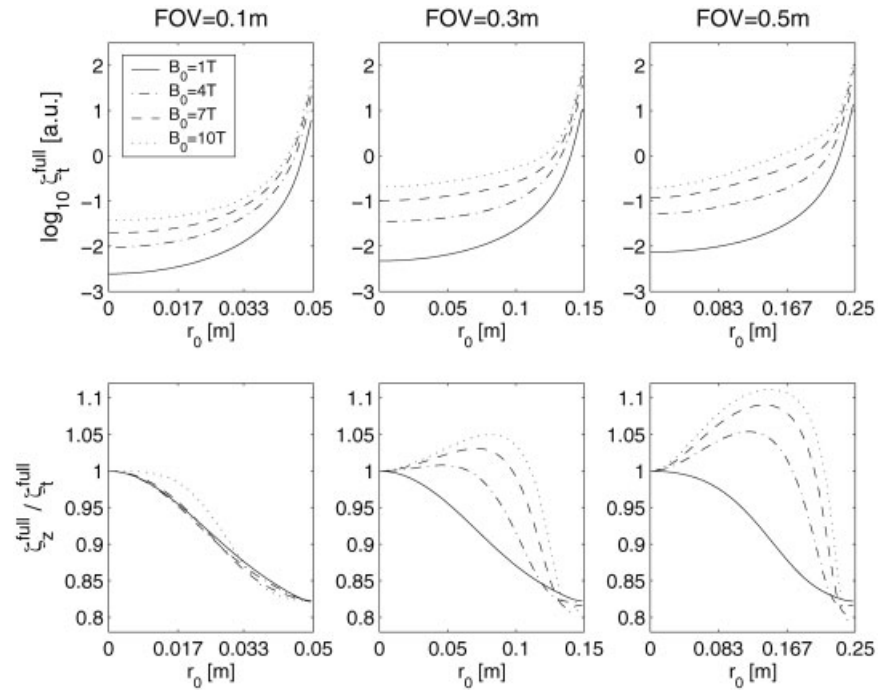
with  $n = 1$  for low  $B_0$  and  $n > 1$  for high  $B_0$ ,  $c$  denoting an individual constant. As suggested by the logarithmic form of Eq. [27], such behavior is best revealed in a double-logarithmic representation, in which the slope is equal to the expo-

nent  $n$ . Hence, in order to verify a similar model for the ultimate SNR, Fig. 6 shows double-logarithmic plots of  $\zeta^{\text{full}}(B_0)$ , for  $B_0$  ranging from 0.5 T to 12 T. Three different positions in the central transverse plane were investigated for several object sizes. For the plots in the upper row, the conductivity was set to average in vivo brain values, whereas for the lower plots approximately lossless conditions ( $\sigma = 10^{-5}(\Omega\text{m})^{-1}$ ) were assumed for comparison.

For all of these situations, the corresponding plots have in common that they are approximately linear for low  $B_0$ , with slopes  $n$  close to 1. Hence, the ultimate SNR is indeed an approximately linear function of  $B_0$  in that regime. For the peripheral position ( $r_0 = 0.95 \cdot \text{FOV}/2$ ), this behavior persists throughout the entire  $B_0$  range. For the other, deeper positions, a transition to a second regime with greater slope is observed. The transition generally occurs sooner for larger objects/FOVs and deeper target positions. This illustrates that the two types of SNR behavior in fact correspond to the two fundamental distance regimes of RF fields. The near field is dominated by evanescent field components, which are of high amplitude but decay rapidly with the distance from the source. The extent of the near-field zone is roughly equal to the RF wavelength, which is inversely proportional to  $B_0$ . Hence, MR detection is near-field dominated at low  $B_0$  or from positions close to the object's surface. The far field consists of propagating field components, which hence are the carriers of MR detection at high  $B_0$  or from positions far away from the surface.

For more quantitative analysis, the near- and far-field exponents,  $n_{\text{NF}}$  and  $n_{\text{FF}}$ , were determined from the data plotted in Fig. 6. This analysis was performed by linear regression of the individual curve segments corresponding to either near- or far-field behavior (Table 2). The linear segments for regression analysis were identified visually and are indicated in Fig. 6. In several cases either the near- or the far-field regression could not be performed because the sampled  $B_0$  range did not sufficiently cover the respective regime. For instance, the superficial position shows only near-field behavior throughout, hence not yielding a value for  $n_{\text{FF}}$ . Entries missing for this reason are indicated by a dash in Table 2.

FIG. 5. Ultimate SNR in conventional MRI as a function of the position in the sphere. The top row shows the ultimate SNR along an arbitrary radius in the transverse plane ( $\zeta_t^{\text{full}}$ ), for varying object size (= FOV) and  $B_0$ . The ultimate SNR is different along the z axis, which is aligned with  $B_0$ . This is illustrated in the bottom row, showing the relative asymmetry  $\zeta_z^{\text{full}}/\zeta_t^{\text{full}}$ . Note that this ratio always converges to  $\sim 0.82$ , independent of the FOV and  $B_0$ .



The numbers show that the near-field exponent is almost exactly equal to 1 for the lossless case. It is only somewhat smaller than 1 for the conductive object, reflecting increasing losses as the Larmor frequency increases (cf. Fig. 3). As opposed to that, the far-field exponent was found to strongly depend on the object's conductivity. In the lossless case  $n_{\text{FF}}$  was approximately equal to 2.8, irrespective of the object size and the depth of the target position, marking a nearly cubic dependence of ultimate SNR on  $B_0$ . In the lossy sample, the values of  $n_{\text{FF}}$  were

significantly reduced and varied between 1.45 and 2.05, depending on the absolute depth of the target position. Again, the monotonic increase of the tissue conductivity with frequency (cf. Fig. 3) results in reduced SNR gains compared to the lossless case.

#### Ultimate Geometry Factor

Figure 7 shows maps of the ultimate geometry factor in the transverse plane. It covers each combination of four reduc-

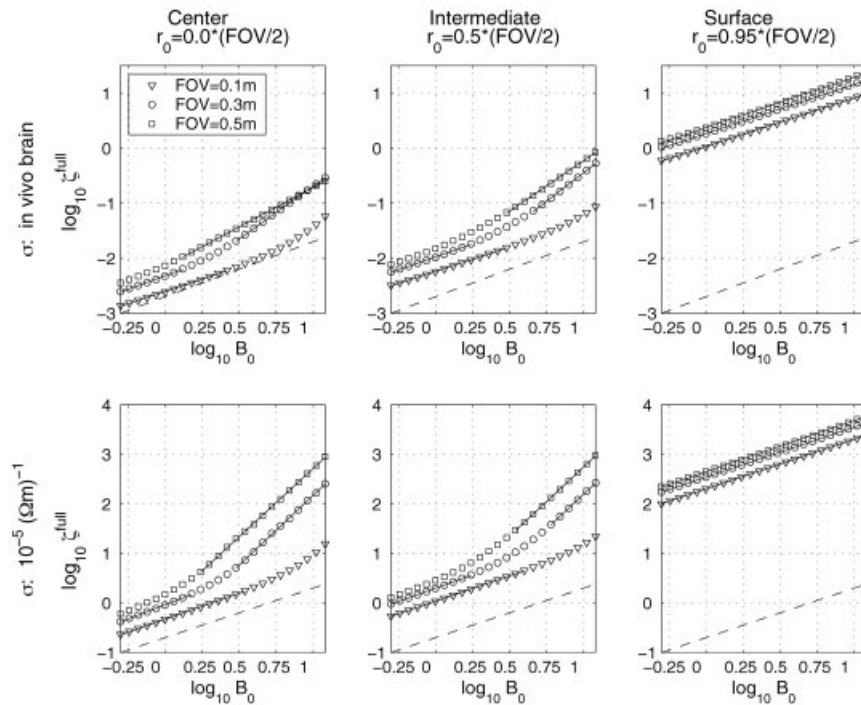


FIG. 6. Ultimate SNR in conventional MRI as a function of  $B_0$ , for three positions in the transverse plane (center, intermediate radius, beneath the surface) and three different object sizes with matching FOV. The dielectric constant was set to frequency-dependent in vivo brain values. The conductivity was likewise set to in vivo values (top row) or to a negligible level for comparison (bottom row). Linear segments in the double-logarithmic plots are emphasized by regression lines. The slope of these segments characterizes the growth of the ultimate SNR as a power of  $B_0$  (see Table 2). For reference, the unit slope corresponding to linear growth of the SNR is indicated by dashed lines.



Table 2

Exponents Describing the Growth of the Ultimate SNR as a Power of  $B_0$ , as Obtained by Linear Regression Analysis of the Results Shown in Fig. 6

	$r_0 = 0.0^*(\text{FOV}/2)$	$r_0 = 0.5^*(\text{FOV}/2)$	$r_0 = 0.95^*(\text{FOV}/2)$
$n_{\text{NF}}$ (avg. brain)	[0.89, 0.99, -]	[0.87, 0.91, -]	[0.89, 0.90, 0.93]
$n_{\text{FF}}$ (avg. brain)	[-, 1.92, 1.45]	[-, 2.05, 1.85]	[-, -, -]
$n_{\text{NF}}$ ( $\sigma \approx 0$ )	[1.03, 1.16, -]	[1.02, 1.07, -]	[1.00, 1.01, 1.04]
$n_{\text{FF}}$ ( $\sigma \approx 0$ )	[-, 2.82, 2.78]	[-, 2.78, 2.80]	[-, -, -]

The three values in each bracket correspond to object sizes and corresponding FOVs of 0.1 m, 0.3 m, and 0.5 m. The exponents differ significantly between the near-field ( $n_{\text{NF}}$ ) and the far-field ( $n_{\text{FF}}$ ) regimes. Missing values indicate that the corresponding regime could not be analyzed within the covered range of  $B_0$ . First section: average brain conductivity. Second section: lossless sample ( $\sigma \approx 0$ ).

tion factors ( $R = 3-6$ ), three object sizes ( $\text{FOV} = 0.1-0.5$  m), and four different field strengths ( $B_0 = 1-10$  T). These results reveal that the performance of parallel imaging is inherently limited. They show that, even with a hypothetical complete coil array, noise enhancement as reflected by the geometry factor cannot be avoided. While the ultimate  $g$  is generally near-optimal ( $g \approx 1$ ) for  $R = 3$  and still fairly low for  $R = 4$ ,

unfavorably high  $g$  factors occur at  $R = 5$  and  $R = 6$ . At these reduction factors the SNR efficiency begins to deteriorate. The strongest increases in  $g$  factor are observed for low field strength and small FOV, whereas at high field and with large FOV the situation remains favorable.

The maps of the ultimate  $g$ -factor tend to have an ovoid structure with a longer extension in the phase-encoding

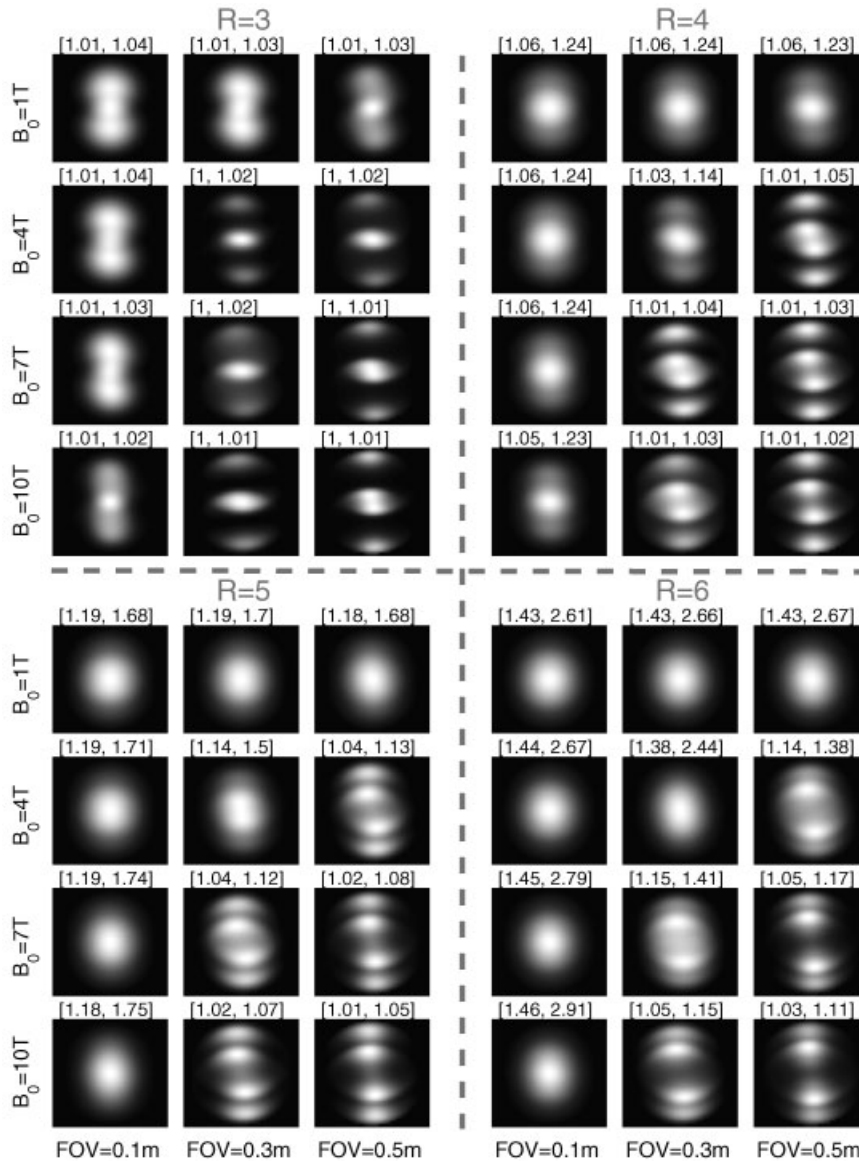
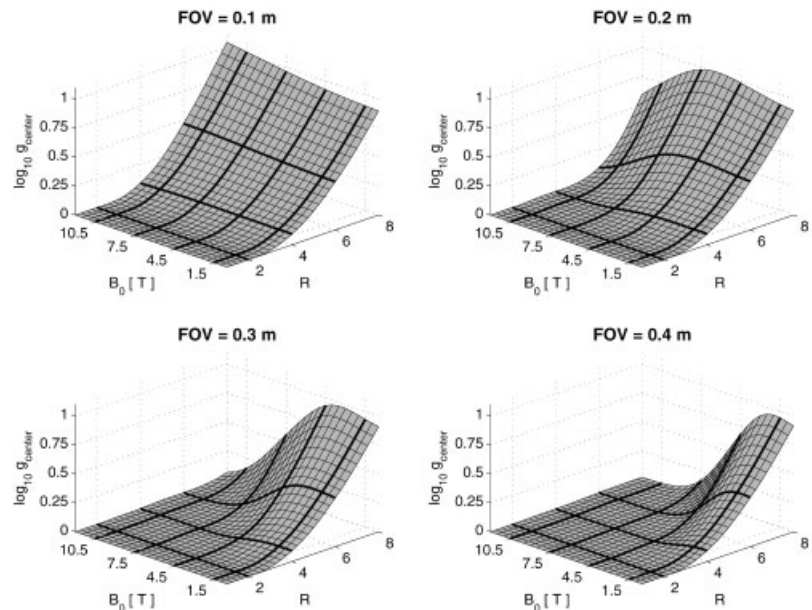


FIG. 7. Maps of the ultimate geometry factor in the transverse plane for  $R = 3$  (top left),  $R = 4$  (top right),  $R = 5$  (bottom left), and  $R = 6$  (bottom right).  $B_0$  was set to 1 T (top rows), 4 T (second rows), 7 T (third rows), and 10 T (bottom rows). The object size and FOV were set to 0.1 m (left columns), 0.3 m (middle columns), and 0.5 m (right columns). The gray scale was individually adjusted to the actual range of  $g$  values. Above each map, the mean and the maximum of  $g$  are indicated in brackets. The geometry factor is a measure of noise enhancement specific to parallel imaging reconstruction. Hence, these results demonstrate that the performance of parallel imaging is inherently limited by electrodynamics. Even with a hypothetical optimal coil array, noise enhancement will occur.

FIG. 8. The ultimate geometry factor in the center of the sphere as a function of the reduction factor  $R$  and  $B_0$ , for various object sizes with corresponding FOV. Two clearly distinct regimes are observed. For low reduction factors or sufficiently large  $B_0$  and FOV the ultimate  $g$  factor is benign with values very close to the optimum of 1. For high reduction factors beyond a critical value, the ultimate  $g$  increases exponentially as a function of  $R$ . This behavior characterizes an unfavorable regime where parallel imaging is strongly hampered by deteriorating SNR efficiency. The transition is approximately at  $R = 4$  in near-field conditions (low  $B_0$ /small FOV) and shifts towards higher reduction factors in far-field conditions (high  $B_0$ /large FOV).



direction. This reflects the fact that the number of aliasing positions within the sphere decreases gradually when  $\mathbf{r}_0$  is shifted away from the center in the frequency-encoding direction. With favorably large  $B_0$  and FOV, the  $g$  maps exhibit characteristic patterns reminiscent of the aliasing that results from Fourier reconstruction alone. In the unfavorable cases of strong reduction at low  $B_0$  and small FOV, the structure of the  $g$  maps is simpler, exhibiting more or less a single blob. As opposed to  $\zeta^{\text{full}}$ , whose minimum was always in the sphere's center, the highest ultimate  $g$  factor does not generally occur in the center. Moreover, equally unlike  $\zeta^{\text{full}}$ , the ultimate  $g$  factor does not exhibit rotational symmetry about the  $z$  axis. This symmetry is broken by the choice of the phase-encoding direction. The only symmetry remaining is with respect to  $z$ -rotation about  $180^\circ$ . Note in particular that the  $g$  maps exhibit slight asymmetries with respect to both the phase and the frequency encoding axes.

According to the previous results, the center region of the sphere is a sensitive marker for the overall feasibility of parallel imaging. First,  $\zeta^{\text{full}}$  always assumed its minimum in the center. Second,  $g$  also assumed its maximum in the center when this maximum was critically high. Therefore, the center position was selected for a more detailed analysis of  $g$  as a function of the field strength and the object size. Figure 8 shows logarithmic plots of the ultimate  $g$  factor vs.  $B_0$  (0.5–12 T) and vs. the reduction factor  $R$  (1–8) for object sizes and corresponding FOVs of 0.1–0.4 m. These graphs further elucidate the transitions previously observed in the  $g$  maps. We can generally distinguish two domains with opposite parallel imaging characteristics. The first, favorable domain is characterized by ultimate  $g$  close to 1 ( $\log g \approx 0$ ), reflecting optimal ultimate parallel imaging performance. The second, unfavorable domain is characterized by exponential growth of the  $g$  factor as a function of  $R$ , which is highly limiting in view of generally limited baseline SNR. In fact, for most applications the onset of the exponential regime will mark a practical up-

per bound to the feasible reduction factor. The transition between the two domains depends on  $B_0$  and the FOV, indicating that it is again governed by the near- and far-field behavior of the involved RF fields. In near-field conditions, i.e., for low  $B_0$  / small FOV, the critical transition is approximately at  $R = 4$  and nearly independent of  $B_0$  and the FOV. In the far-field regime, i.e., for high  $B_0$  / large FOV, the critical transition occurs at a larger  $R$  value, which increases both with  $B_0$  and the FOV.

## DISCUSSION

### Model Assumptions

In this work, practical procedures were developed for studying the electrodynamic limits of the SNR in parallel imaging. In order to keep these procedures numerically feasible, the underlying model was subject to several simplifications.

First, the SNR model is based on the common assumptions of steady-state oscillation and linear response of the detector. The assumption of steady-state oscillation is warranted when the signal bandwidth is significantly smaller than the intrinsic bandwidth of the detector circuit (20). This is usually the case for MRI situations. Linear response is required for using the reciprocity principle as well as for the subsequent linear-algebraic reasoning. This is also a safe assumption for the coils and lumped components typically used in MR detection. Note that the common mechanisms of coil-to-coil coupling, be it inductive, capacitive, or resistive, are likewise linear. The detector electronics often involve components with potentially nonlinear behavior, such as switching diodes or transistors for preamplification. However, the circuitry is generally designed to use these components in a linear regime of operation to avoid distortion and intermodulation. After all, linear overall detector response is a prerequisite for applying the common Fourier principles at the data-processing stage.

In setting up the Maxwell equations, it was assumed that the imaged object was source-free, homogeneous, and spherical in shape. The absence of sources corresponds to all RF coils being placed outside the object, which is realistic for most MRI procedures. Electromagnetic homogeneity is an accurate assumption for simple phantoms, while it represents only a first approximation to in vivo situations. In order to approximate the conditions of head imaging, the electromagnetic constants were modeled as frequency-dependent and set to average in vivo brain values. With such a description, the main phenomena such as near-field and far-field wave behavior as well as dissipation can be realistically modeled. The local tissue structure becomes most critical only at very high frequencies, where it may give rise to specific RF resonances. In terms of shape, too, the spherical model, with appropriate radius, may be regarded as a first approximation of a human head. Furthermore, the sphere may be regarded as a worst-case situation for parallel imaging, as it maximizes the mean distance to the surface for a given volume.

Clearly, the model results cannot be expected to directly apply to in vivo situations. However, two points suggest that the main findings may qualitatively translate to practical imaging. First, the results obtained in the homogeneous sphere are highly regular, i.e., they do not change abruptly as a function of  $B_0$ , FOV, or material properties. Hence, it may be expected that they will also change smoothly as the object approaches reality. Second, the model results are qualitatively in line with many in vivo experiments, which showed that the g factor tends to grow critically at acceleration factors beyond three to four.

Concerning the Maxwell equations, a further, more subtle simplification needs to be pointed out. Note that proper electrodynamic behavior was enforced only inside the object, where the transmit fields  $\mathbf{E}$  and  $\mathbf{H}$  affect the SNR immediately. Strictly speaking, this requirement is too weak, as any physically feasible fields will solve the Maxwell equations also outside the object and fulfill boundary conditions at the object's surface. However, these additional conditions effectively do not constrain the solution space inside the object. Intuitively, this can be understood by considering that the outside space may host an arbitrary configuration of coil conductors, which act as current sources in the transmission picture. So there are infinitely many degrees of freedom available for continuing a given Maxwell solution towards the outside in a physically meaningful fashion. This can also be established more formally with methods of inverse source identification, as described, e.g., in Ref. 24. However, due to lack of space a detailed formal treatment of this aspect is left to separate publication. So, strictly speaking, it is an assumption of this work that every physical Maxwell solution inside the object is consistent with a corresponding current distribution on the outside. This implies that the calculated SNR bounds are tight, i.e., that they can be accomplished, at least theoretically, with actual coil conductor distributions. Even if the aforementioned assumption was wrong, the calculated limits would still hold as upper, yet not tight, bounds.

The study focused on the most widely used parallel imaging mode, namely, on Cartesian  $k$ -space sampling with undersampling in one dimension. However, the

model and algorithms apply without modification to the Cartesian case with undersampling in two or three dimensions. Based on experimental findings and straightforward geometrical considerations (19), it is expected that the critical reduction factors will be significantly higher for 2D and 3D undersampling than for the elementary 1D case studied in this work. The transition to non-Cartesian sampling with, e.g., spirals, is less simple. With general  $k$ -space patterns, the point-spread function can no longer be viewed as a set of discrete peaks. As a consequence, the concept of net sensitivity no longer applies in the simple form used for the Cartesian case. Hence, in order to analyze non-Cartesian parallel imaging, more advanced reconstruction approaches must be incorporated (25,26). By analogy with the findings of the present work, the ultimate SNR can then be assessed by applying these reconstruction methods to a hypothetical complete coil array.

### Basis Functions and Different Types of Wave Behavior

The choice of an appropriate Maxwell basis is crucial for the accurate calculation of ultimate SNR. On the one hand, each basis element must be a Maxwell solution and the basis as a whole must be approximately complete. On the other hand, the number of basis elements is constrained by limited computing resources. In combination with the spherical object, vector spherical harmonics have proven numerically efficient in the present work. A more straightforward choice is a plane wave expansion (27,28) as previously used in Refs. 11, 12, and 29. It is formally simpler than the spherical expansion, yet it has the drawback of requiring a particularly large number of basis functions, as briefly discussed in the following.

Standard plane wave approaches (27,28) are based on a Fourier expansion of the electromagnetic field in the  $x$ - $y$  plane, constructing a plane wave from each element of 2D  $k$ -space. For any pair of real numbers,  $(k_x, k_y)$ , a plane wave with wave vector  $\mathbf{k}$  is defined by choosing the remaining component,  $k_z$ , such as to fulfill the Helmholtz equation [14]:

$$k_0^2 = k_x^2 + k_y^2 + k_z^2. \quad [28]$$

This equation ensures that the corresponding wave oscillates and decays according to  $k_0$ , the material's wave number at the respective frequency. When all components of  $\mathbf{k}$  have the same phase the situation simplifies in that the magnitude of  $\mathbf{k}$  becomes equal to that of  $k_0$ . This assumption was used in the original article on ultimate SNR (12), as well as in Ref. 11, reducing the size of the plane wave basis in favor of more efficient computation. However, it is important to note that  $k_z$  does not need to be in phase with  $k_x$ ,  $k_y$ , and Eq. [28] has solutions for all pairs  $(k_x, k_y)$ . In particular, the magnitude of the wave vector is not limited by the magnitude of  $k_0$ . Note also that the plane waves constructed in this fashion are linearly independent, which is reflected by the fact that they form a common Fourier basis in the  $x$ - $y$  plane. As a consequence, for creating a complete plane wave basis the pairs  $(k_x, k_y)$  must cover all of 2D  $k$ -space. In practice, the relevant range of wave vectors is limited by the desired spatial resolution of the study. However, for typical MRI situations with  $k$ -



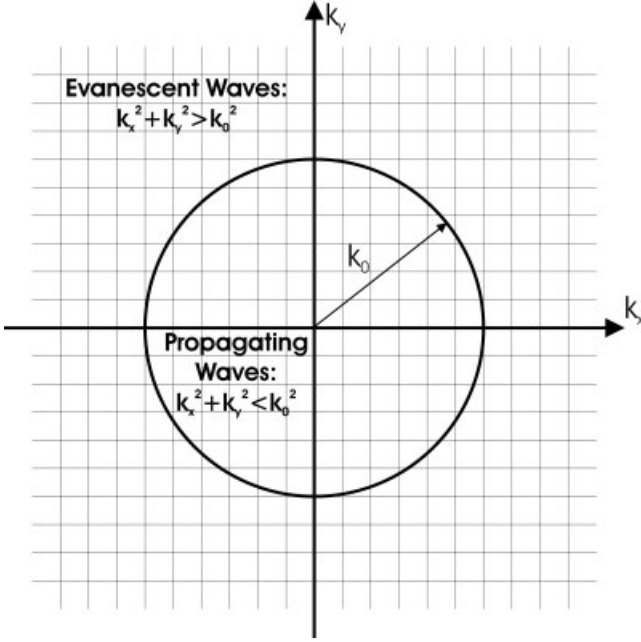


FIG. 9. The components of a plane wave expansion can be categorized into evanescent and propagating waves. The distinction is clearest in the case of a lossless sample with real-valued wave number  $k_0$ . In this case, the evanescent components are characterized by wave vectors  $\mathbf{k}$  with  $k_x^2 + k_y^2 > k_0^2$  and imaginary  $k_z$ , causing evanescence, i.e., exponential decay in the  $z$  direction. Plane waves with  $k_x^2 + k_y^2 < k_0^2$  have a real  $k_z$ -component and extend indefinitely in all directions.

space sampling up to, say,  $k_{\max} = 1 \text{ mm}^{-1}$ , this limit is still orders of magnitude larger than  $k_0$ , leading to basis sets of daunting size. This problem is inherent to plane wave bases and not different when starting from  $k_x$ - $k_z$ -, or  $k_y$ - $k_z$ -space and solving Eq. [28] for  $k_y$  or  $k_x$ , respectively.

Equation [28] is also useful for illustrating near- and far-field behavior as observed in the present work. After calculating  $k_z$  for a pair  $(k_x, k_y)$ , the real and imaginary parts of  $k_z$  reflect oscillation and decay, respectively, along the  $z$  direction. This distinction is clearest for a lossless sample, in which the wave number  $k_0$  is purely real. According to Eq. [28],  $k_z$  then is either purely real or purely imaginary. As depicted in Fig. 9, these two situations correspond to two distinct domains in the  $k_x$ - $k_y$ -plane, which are separated by a circle with radius  $k_0$ . Within the circle  $k_z$  is real; the corresponding plane waves extend indefinitely in all directions, contributing to the far field. Outside the circle  $k_z$  is imaginary, marking so-called evanescent waves that decay exponentially in the  $z$  direction. Evanescent waves form the near field of an oscillating source, which reaches up to a distance of approximately one wavelength (28). Hence, the signal detection in MRI is usually near-field-dominated (18), in particular when using surface coils for SNR optimization. In fact, Biot-Savart's law, which is frequently used for calculating receiver coil sensitivities, accounts exclusively for near-field components (15). Nevertheless, as shown in the present work, far-field behavior can be relevant in large objects and at high  $B_0$ . This illustrates that ultimate SNR calculations should fully capture both near- and far-field behavior,

requiring a complete Maxwell basis such as full plane waves or the vector spherical harmonics used in the present work.

#### Coil Optimality for Parallel and Conventional Imaging

An important question in coil design is whether an array that is optimized for parallel imaging will also perform well in conventional imaging with full Fourier encoding and vice versa. In Ref. 10, Reykowski et al. previously suggested that an array should be optimal for SENSE imaging of a given pixel if it contains optimal coils for conventional imaging of each pixel involved in the aliasing process. Based on the theoretical considerations in the present work, this can be formally confirmed and somewhat generalized. For an arbitrary set of aliasing positions, let the vector  $\mathbf{s}_\rho$  denote the  $\rho$ -th column of the corresponding sensitivity matrix (Eq. [20]) and  $\mathbf{w}_\rho^{\text{SENSE}}$  the  $\rho$ -th row of the optimal weighting matrix according to Eq. [24]. The latter can then be written as:

$$\begin{pmatrix} \mathbf{w}_0^{\text{SENSE}} \\ \mathbf{w}_1^{\text{SENSE}} \\ \vdots \\ \mathbf{w}_N^{\text{SENSE}} \end{pmatrix} = \begin{pmatrix} * & * & \dots & * \\ * & * & \dots & * \\ \vdots & \vdots & \ddots & \vdots \\ * & * & \dots & * \end{pmatrix} \begin{pmatrix} \mathbf{s}_0^H \Psi^{-1} \\ \mathbf{s}_1^H \Psi^{-1} \\ \vdots \\ \mathbf{s}_N^H \Psi^{-1} \end{pmatrix}, \quad [29]$$

where the asterisks indicate that the entries of the matrix in the middle are not relevant for the following argument. For comparison, the SNR at the same positions can also be optimized for conventional imaging without aliasing. For the pixel with index  $\rho$ , Eq. [24] then simplifies to:

$$\mathbf{w}_\rho^{\text{CONV}} = (*) \mathbf{s}_\rho^H \Psi^{-1}, \quad [30]$$

where the asterisk again replaces an irrelevant factor. Combining Eqs. [29,30] yields:

$$\begin{pmatrix} \mathbf{w}_0^{\text{SENSE}} \\ \mathbf{w}_1^{\text{SENSE}} \\ \vdots \\ \mathbf{w}_N^{\text{SENSE}} \end{pmatrix} = \begin{pmatrix} * & * & \dots & * \\ * & * & \dots & * \\ \vdots & \vdots & \ddots & \vdots \\ * & * & \dots & * \end{pmatrix} \begin{pmatrix} \mathbf{w}_0^{\text{CONV}} \\ \mathbf{w}_1^{\text{CONV}} \\ \vdots \\ \mathbf{w}_N^{\text{CONV}} \end{pmatrix}. \quad [31]$$

This equation confirms that the ideal coils for conventional imaging and the ideal net coils for SENSE reconstruction are connected by a simple linear mapping. By this mapping and its inverse, it is possible to convert data obtained with either coil set into virtual data that are exactly equal to what would have been obtained with the other coil set. In other words, both coil sets span the same space of feasible net coils and are thus equivalent at the level of SENSE reconstruction. Hence, a coil array that is optimal for the separation of given aliasing positions in SENSE imaging is also optimal at each of these positions for conventional imaging and vice versa.

#### CONCLUSIONS

In the present work, inherent limits of parallel MR imaging were studied by analyzing the impact of the underlying



electrodynamics on the achievable SNR. The key findings are the following:

1) The range of reasonable reduction factors in parallel imaging is fundamentally limited by electrodynamics. For low and moderate reduction factors, the ultimate geometry factor is close to its optimal value of 1. However, for high reduction factors beyond a critical value, the ultimate  $g$  factor tends to increase exponentially, marking a regime where parallel imaging is strongly hampered by deteriorating SNR efficiency. This limitation cannot be circumvented by enhanced coil design, as long as the coils are bound to stay outside of the object.

2) The critical reduction factor behaves differently in the near- and far-field regimes of the detected RF fields. In the near-field regime, i.e., for low  $B_0$  / small objects, the critical reduction factor is independent of  $B_0$  and the object size and approximately equal to 4 for 1D reduction in a sphere. In the far-field regime, i.e., for high  $B_0$  / large objects, the critical reduction factor is generally larger and increases with both  $B_0$  and the object size. For a head-sized object with in vivo properties, the transition between the two regimes is at  $\sim 5$  T. Similar transitions were observed for conventional MRI with full  $k$ -space sampling. Hence, at very high field strengths such as 7 T and beyond, both parallel and conventional imaging in humans is expected to benefit significantly from far-field behavior.

## ACKNOWLEDGMENTS

The authors thank Dr. Pascal Leuchtmann from the Laboratory for Electromagnetic Fields and Microwave Electronics of the Swiss Federal Institute of Technology, Zurich, for helpful discussions regarding electrodynamics.

## APPENDIX A

### Minimum-Norm Formulation of SNR Optimization

In the Theory section, the problem of optimizing the SNR for a set of aliasing pixels was expressed as that of minimizing the cost functional:

$$\Delta = \text{Tr}(\mathbf{W}\Psi\mathbf{W}^H) \quad [\text{A1}]$$

by variation of the weighting matrix  $\mathbf{W}$  under the linear constraint

$$\mathbf{W}\mathbf{S} = \text{Id}, \quad [\text{A2}]$$

where  $\text{Tr}$  denotes the trace operator and  $\text{Id}$  denotes the  $(N+1) \times (N+1)$  identity matrix. In order to cast the minimization of  $\Delta$  into the form of a minimum-norm problem, the noise covariance matrix is eliminated by transforming the weighting matrix. Note that, for linearly independent electrical basis functions  $\boldsymbol{\alpha}_m(\mathbf{r})$ ,  $\Psi$  is positive-definite, thus permitting the Cholesky factorization (30):

$$\Psi = \mathbf{L}\mathbf{L}^H. \quad [\text{A3}]$$

Transforming the weighting vector and the sensitivity matrix by the root  $\mathbf{L}$ :

$$\tilde{\mathbf{W}} = \mathbf{W}\mathbf{L} \quad [\text{A4}]$$

$$\tilde{\mathbf{S}} = \mathbf{L}^{-1}\mathbf{S}, \quad [\text{A5}]$$

the cost functional and the constraint in Eqs. [A1, A2] can be rewritten as:

$$\Delta = \text{Tr}(\tilde{\mathbf{W}}\tilde{\mathbf{W}}^H) \quad [\text{A6}]$$

$$\tilde{\mathbf{W}}\tilde{\mathbf{S}} = \text{Id}. \quad [\text{A7}]$$

According to this formulation, the optimal  $\tilde{\mathbf{W}}$  is the minimum-norm solution of Eq. [A7], which can be calculated by means of the Moore-Penrose pseudoinverse of  $\tilde{\mathbf{S}}$  (30):

$$\tilde{\mathbf{W}}_{\min} = \tilde{\mathbf{S}}^+ = (\tilde{\mathbf{S}}^H\tilde{\mathbf{S}})^{-1}\tilde{\mathbf{S}}^H \quad [\text{A8}]$$

The latter equality holds if the rank of  $\tilde{\mathbf{S}}$  is equal to its width. This will generally be the case with a number of Maxwell basis functions much larger than the number of aliasing pixels. Transforming  $\tilde{\mathbf{W}}_{\min}, \tilde{\mathbf{S}}$  back to the original coordinates yields the optimal weighting vector:

$$\mathbf{W}_{\min} = (\mathbf{S}^H\Psi^{-1}\mathbf{S})^{-1}\mathbf{S}^H\Psi^{-1}. \quad [\text{A9}]$$

## APPENDIX B

### Multipole Expansion

The multipole expansion used in this work was constructed as follows. Each solution of the homogeneous and source-free Maxwell Eqs. [13] can be expressed in spherical coordinates as (20,22,31):

$$\begin{aligned} \mathbf{H}(\mathbf{r}, \theta, \varphi) = \sum_{l=0}^{\infty} \sum_{m=-l}^l \left\{ w_{l,m}^E j_l(k_0 r) \mathbf{X}_{l,m}(\theta, \varphi) \right. \\ \left. - \frac{i}{k_0} w_{l,m}^M \nabla \times [j_l(k_0 r) \mathbf{X}_{l,m}(\theta, \varphi)] \right\} \\ \mathbf{E}(\mathbf{r}, \theta, \varphi) = \frac{\omega\mu}{k_0} \sum_{l=0}^{\infty} \sum_{m=-l}^l \left\{ \frac{i}{k_0} w_{l,m}^E \nabla \times [j_l(k_0 r) \mathbf{X}_{l,m}(\theta, \varphi)] \right. \\ \left. + w_{l,m}^M j_l(k_0 r) \mathbf{X}_{l,m}(\theta, \varphi) \right\}. \quad [\text{B1}] \end{aligned}$$

Here,  $w_{l,m}^E$  and  $w_{l,m}^M$  denote expansion coefficients of electric-source and magnetic-source multipole basis functions, respectively.  $j_l$  denotes the  $l$ -th spherical Bessel function of the first kind and  $\mathbf{X}_{l,m}$  the vector spherical harmonics, which can be expressed as (20,22,31):

$$\mathbf{X}_{l,m}(\theta, \varphi) = \frac{-i}{\sqrt{l(l+1)}} (\hat{\mathbf{r}} \times \nabla) Y_{l,m}(\theta, \varphi), \quad [\text{B2}]$$

where  $\hat{\mathbf{r}}$  denotes a unit vector in the radial direction and  $Y_{l,m}$  are the common scalar spherical harmonics. Expanding the rotation terms in Eq. [B1] (22,31):

$$\nabla \times [\mathbf{j}_l(k_0 \mathbf{r}) \mathbf{X}_{l,m}(\theta, \varphi)] = \frac{1}{r} \frac{\partial}{\partial r} [\mathbf{r} \mathbf{j}_l(k_0 \mathbf{r})] \hat{\mathbf{r}} \times \mathbf{X}_{l,m}(\theta, \varphi) + i \sqrt{l(l+1)} \frac{j_l(k_0 r)}{r} Y_{l,m}(\theta, \varphi) \hat{\mathbf{r}} \quad [\text{B3}]$$

yields a favorable representation of the multipole expansion [B1] as a sum of three terms:

$$\begin{aligned} \mathbf{H}(\mathbf{r}) = \sum_{l=0}^{\infty} \sum_{m=-l}^l \left\{ \mathbf{w}_{l,m}^E j_l(k_0 r) \mathbf{X}_{l,m} - \mathbf{w}_{l,m}^M \left[ \frac{i}{k_0 r} \frac{\partial [\mathbf{r} \mathbf{j}_l(k_0 \mathbf{r})]}{\partial r} \hat{\mathbf{r}} \times \mathbf{X}_{l,m} - \frac{\sqrt{l(l+1)}}{k_0 r} j_l(k_0 r) Y_{l,m} \hat{\mathbf{r}} \right] \right\} \\ \mathbf{E}(\mathbf{r}) = \frac{\omega \mu}{k_0} \sum_{l=0}^{\infty} \sum_{m=-l}^l \left\{ \mathbf{w}_{l,m}^E \left[ \frac{i}{k_0 r} \frac{\partial [\mathbf{r} \mathbf{j}_l(k_0 \mathbf{r})]}{\partial r} \hat{\mathbf{r}} \times \mathbf{X}_{l,m} - \frac{\sqrt{l(l+1)}}{k_0 r} j_l(k_0 r) Y_{l,m} \hat{\mathbf{r}} \right] + \mathbf{w}_{l,m}^M j_l(k_0 r) \mathbf{X}_{l,m} \right\}. \quad [\text{B4}] \end{aligned}$$

The individual terms obey the following orthogonality relations:

$$\begin{aligned} \int Y_{l,m} Y_{l',m'}^* d\Omega = \delta_{l,l'} \delta_{m,m'} \quad \int (\hat{\mathbf{r}} \times \mathbf{X}_{l,m}) \cdot \hat{\mathbf{r}} Y_{l',m'}^* d\Omega = 0 \\ \int \mathbf{X}_{l,m} \cdot \mathbf{X}_{l',m'}^* d\Omega = \delta_{l,l'} \delta_{m,m'} \quad \int (\hat{\mathbf{r}} \times \mathbf{X}_{l,m}) \cdot \mathbf{X}_{l',m'}^* d\Omega = 0 \\ \int (\hat{\mathbf{r}} \times \mathbf{X}_{l,m}) \cdot (\hat{\mathbf{r}} \times \mathbf{X}_{l',m'}^*) d\Omega = \delta_{l,l'} \delta_{m,m'} \\ \int \mathbf{X}_{l,m} \cdot \hat{\mathbf{r}} Y_{l',m'}^* d\Omega = 0, \quad [\text{B5}] \end{aligned}$$

where  $\int d\Omega$  indicates integration over the surface of the unit sphere.

For numerical calculations, the order of the expansion must be limited to  $l \leq l_{\max}$ , yielding  $2(l_{\max}+1)^2$  basis functions in total. The corresponding set of weighting coefficients  $w_{l,m}^E$  and  $w_{l,m}^M$  were assembled in the weighting vector  $\mathbf{w}$ , using the following convention:

$$\mathbf{w} = (w_{0,0}^E, w_{1,-1}^E, w_{1,0}^E, w_{1,1}^E, \dots, w_{l_{\max}, l_{\max}-1}^E, w_{l_{\max}, l_{\max}}^E, w_{0,0}^M, w_{1,-1}^M, w_{1,0}^M, w_{1,1}^M, \dots, w_{l_{\max}, l_{\max}-1}^M, w_{l_{\max}, l_{\max}}^M). \quad [\text{B6}]$$

Using the same convention and exploiting the orthogonality relations [B5], the noise covariance matrix  $\Psi$  (see Eq. [22]) assumes a convenient diagonal form:

$$\Psi = \left| \frac{\omega \mu}{k_0} \right|^2 \begin{pmatrix} \Psi^E & 0 \\ 0 & \Psi^M \end{pmatrix}, \quad \text{where}$$

$$\Psi_{(l,m),(l',m')}^E = \delta_{l,l'} \delta_{m,m'} \left| \frac{1}{k_0} \right|^2 \int_{r=0}^{\text{FOV}/2} \left[ \left| \frac{\partial (\mathbf{r} \mathbf{j}_l(k_0 \mathbf{r}))}{\partial r} \right|^2 + l(l+1) |j_l(k_0 r)|^2 \right] dr$$

$$\Psi_{(l,m),(l',m')}^M = \delta_{l,l'} \delta_{m,m'} \int_{r=0}^{\text{FOV}/2} r^2 |j_l(k_0 r)|^2 dr. \quad [\text{B7}]$$

$\Psi^E$  involves analytically unknown integrals, which were solved using Gauss quadrature.

The corresponding signal sensitivity matrix (see Eq. [20]) is given by:

$$\mathbf{S} = \begin{pmatrix} \mathbf{S}^{E,x} - i \mathbf{S}^{E,y} \\ \mathbf{S}^{M,x} - i \mathbf{S}^{M,y} \end{pmatrix}, \quad \text{where}$$

$$\mathbf{S}_{(l,m),\rho}^{E,x} = j_l(k_0 r_\rho) [\mathbf{X}_{l,m}(\theta_\rho, \varphi_\rho)]_x$$

$$\begin{aligned} \mathbf{S}_{(l,m),\rho}^{M,x} = - \frac{i}{k_0 r_\rho} \frac{\partial [\mathbf{r} \mathbf{j}_l(k_0 \mathbf{r})]}{\partial r} \bigg|_{r=r_\rho} [\hat{\mathbf{r}}_\rho \times \mathbf{X}_{l,m}(\theta_\rho, \varphi_\rho)]_x \\ + \frac{\sqrt{l(l+1)}}{k_0 r_\rho} j_l(k_0 r_\rho) Y_{l,m}(\theta_\rho, \varphi_\rho) [\hat{\mathbf{r}}_\rho]_x. \quad [\text{B8}] \end{aligned}$$

$\mathbf{S}^{E,y}$  and  $\mathbf{S}^{M,y}$  are defined analogously, using the respective y-components.  $r_\rho, \theta_\rho, \psi_\rho$  denote the spherical representation of the  $\rho$ -th aliasing position  $\mathbf{r}_\rho$ .

## REFERENCES

1. Sodickson DK, Manning WJ. Simultaneous acquisition of spatial harmonics (SMASH): fast imaging with radiofrequency coil arrays. *Magn Reson Med* 1997;38:591–603.
2. Jakob PM, Griswold MA, Edelman RR, Sodickson DK. AUTO-SMASH: a self-calibrating technique for SMASH imaging. *Simultaneous Acquisition of Spatial Harmonics*. MAGMA 1998;7:42–54.
3. Pruessmann KP, Weiger M, Scheidegger MB, Boesiger P. SENSE: sensitivity encoding for fast MRI. *Magn Reson Med* 1999;42:952–962.
4. Kyriakos WE, Panych LP, Kacher DF, Westin CF, Bao SM, Mulkern RV, Jolesz FA. Sensitivity profiles from an array of coils for encoding and reconstruction in parallel (SPACE RIP). *Magn Reson Med* 2000;44:301–308.
5. Griswold MA, Jakob PM, Heidemann RM, Nittka M, Jellus V, Wang J, Kiefer B, Haase A. Generalized autocalibrating partially parallel acquisition (GRAPPA). *Magn Reson Med* 2002;47:1202–1210.
6. Weiger M, Pruessmann KP, Leussler C, Roschmann P, Boesiger P. Specific coil design for SENSE: a six-element cardiac array. *Magn Reson Med* 2001;45:495–504.
7. Ohliger MA, Greenman R, McKenzie CA, Sodickson DK. Concentric coil arrays for spatial encoding in parallel MRI. In: *Proc 9th Annual Meeting ISMRM*, Glasgow, 2001. p 21.
8. de Zwart JA, Ledden PJ, Kellman P, van Gelderen P, Duyn JH. Design of a SENSE-optimized high-sensitivity MRI receive coil for brain imaging. *Magn Reson Med* 2002;47:1218–1227.
9. Wiesinger F, Pruessmann KP, Boesiger P. Inherent limitation of the reduction factor in parallel imaging as a function of field strength. In: *Proc 10th Annual Meeting ISMRM*, Honolulu, 2002. p 191.
10. Reykowski A, Schnell W, Wang J. Simulation of SNR limit for SENSE related reconstruction techniques. In: *Proc 10th Annual Meeting ISMRM*, Honolulu, 2002. p 2385.

11. Ohliger MA, Grant AK, Sodickson DK. Ultimate intrinsic signal-to-noise ratio for parallel MRI: electromagnetic field considerations. *Magn Reson Med* 2003;50:1018–1030.
12. Ocali O, Atalar E. Ultimate intrinsic signal-to-noise ratio in MRI. *Magn Reson Med* 1998;39:462–473.
13. Hoult DI, Richards RE. The signal-to-noise ratio of the nuclear magnetic resonance experiment. *J Magn Reson* 1976;24:71–85.
14. Hoult DI. The principle of reciprocity in signal strength calculations — a mathematical guide. *Concepts Magn Reson* 2000;12:173–187.
15. Insko EK, Elliott MA, Schotland JC, Leigh JS. Generalized reciprocity. *J Magn Reson* 1998;131:111–117.
16. Johnson JB. Thermal agitation of electricity in conductors. *Phys Rev* 1928;32:97–109.
17. Nyquist H. Thermal agitation of electric charge in conductors. *Phys Rev* 1928;32:110–113.
18. Hoult DI, Bhakar B. NMR signal reception: virtual photons and coherent spontaneous emission. *Concepts Magn Reson Part A* 1997;9:227–297.
19. Weiger M, Pruessmann KP, Boesiger P. 2D SENSE for faster 3D MRI. *MAGMA* 2002;14:10–19.
20. Jackson JD. *Classical electrodynamics*. New York: John Wiley & Sons; 1999.
21. Gabriel S, Lau RW, Gabriel C. The dielectric properties of biological tissues. III. Parametric models for the dielectric spectrum of tissues. *Phys Med Biol* 1996;41:2271–2293.
22. Keltner JR, Carlson JW, Roos MS, Wong ST, Wong TL, Budinger TF. Electromagnetic fields of surface coil in vivo NMR at high frequencies. *Magn Reson Med* 1991;22:467–480.
23. Hoult DI. Sensitivity and power deposition in a high-field imaging experiment. *J Magn Reson Imag* 2000;12:46–67.
24. Bleistein N, Cohen JK. Nonuniqueness in the inverse source problem in acoustics and electromagnetics. *J Math Phys* 1977;18:194–201.
25. Pruessmann KP, Weiger M, Bornert P, Boesiger P. Advances in sensitivity encoding with arbitrary  $k$ -space trajectories. *Magn Reson Med* 2001;46:638–651.
26. Yeh EN, McKenzie CA, Lim D, Ohliger MA, Grant A, Willig J, Rofsky N, Sodickson DK. Parallel imaging with augmented radius in  $k$ -space (PARS). In: *Proc 10th Annual Meeting ISMRM, Honolulu, 2002*. p 2399.
27. Devaney AJ, Wolf E. Multipole expansion and plane wave representations of the electromagnetic field. *J Math Phys* 1974;15:234–244.
28. Goodman JW. *Introduction to Fourier optics*. San Francisco: McGraw-Hill; 1968. p 55–61.
29. Wiesinger F, Pruessmann KP, Boesiger P. Verschiebung der SNR Limitation in der parallelen Bildgebung bei zunehmender Feldstärke. In: *Proc 4th Annual Meeting German Section ISMRM, Zurich (www.mr.ethz.ch/ismrm01/presentation.html) 2001*. p 33.
30. Golub GH, Van Loan CF. *Matrix computations*. Baltimore: Johns Hopkins University Press; 1996.
31. Arfken GB, Weber HJ. *Mathematical methods for physicists*. San Diego: Hartcourt/Academic Press; 2001.